RSC Chemical Biology

ROYAL SOCIETY OF CHEMISTRY

PAPER

View Article Online
View Journal | View Issue

Cite this: *RSC Chem. Biol.*, 2025, 6, 1749

Structural basis of SIRT2 pre-catalysis NAD^+ binding dynamics and mechanism

Nan Zhang, [abc] Kah Chee Pow, [ab] Lanfang Chen[c] and Quan Hao *[ab]

Sirtuins are an evolutionarily conserved family of NAD^+-dependent deacylases whose catalytic mechanism remains under active investigation. While previous studies have captured sirtuin reaction intermediates using thioacetyl-lysine analogs, here we report six crystal structures of human SIRT2 in complex with native myristoylated peptides and NAD^+, revealing the sequence of changes from initial NAD^+ binding to the formation of intermediate I. Our structures provide direct structural evidence for: (1) zinc-binding domain shift during NAD^+ entry, (2) water-mediated hydrogen-bond formation that disrupts nicotinamide aromaticity preceding cleavage, and (3) the formation of intermediate I. Additionally, we determined the structures of two functionally critical mutants ($SIRT2^{F96A}$ and $SIRT2^{H187A}$), demonstrating their roles in stabilizing NAD^+ in a productive conformation. These findings complete the comprehensive structural framework for the sirtuin deacylation mechanism and highlight key residues governing catalytic efficiency.

Received 30th June 2025,
Accepted 31st August 2025

DOI: 10.1039/d5cb00169b

rsc.li/rsc-chembio

Introduction

Histone post-translational modifications (PTMs) involve the dynamic addition ('writing'), recognition ('reading'), or removal ('erasing') of covalent chemical groups on specific histone amino acid residues. These modifications serve as a fundamental epigenetic mechanism that regulates diverse cellular processes, including metabolic regulation,[1] signal transduction[2] and DNA repair.[3]

Sirtuins are eukaryotic homologs of yeast Sir2 (silent information regulator 2), known as histone deacetylase, which catalyzes the removal of an acyl group with the consumption of nicotinamide adenine dinucleotide (NAD^+). As an important PTM eraser, sirtuins are known to remove not only acetyl groups but also many other modifications with diverse chemical properties. These modifications include: (1) hydrophobic groups from short alkane-like propionylation[4] or butyrylation,[5] to long-chain alkanes like palmitoylation, myristoylation,[6,7] *etc.*; (2) acidic groups such as malonylation,[8] succinylation[9] and glutarylation;[10] and (3) polar groups such as lactylation,[11] β-hydroxybutyrylation[12] and 2-hydroxyisobutyrylation.[13]

In *Homo sapiens*, there are seven isoforms of sirtuin, divided into four classes (I–IV) based on phylogenetic analysis.[14] Class I includes SIRT1–3, which, despite their distinct cellular localizations (primarily nucleus,[15] cytoplasm[16] and mitochondria,[17] respectively), are all effective erasers of short hydrophobic acyl groups like acetyl-lysine (Kac, two-carbon alkane)[16] and butyryl-lysine (Kbu, four-carbon alkane).[18] Additionally, SIRT1–3 have been reported to cleave unsaturated hydrophobic acyl groups like crotonyl-lysine (Kcr, four-carbon unsaturated acyl acids).[19,20] Class II consists of SIRT4, a mitochondrial protein that efficiently removes lipoyl-lysine (Klip), biotinyl-lysine (Kbio) and methylglutaryl-lysine modifications.[21,22] Class III includes SIRT5, another mitochondrial protein that preferentially hydrolyzes acidic acyl groups.[8–10] SIRT6 and SIRT7 belong to class IV, and these nuclear proteins both exhibit ADP-ribosyltransferase activity.[23,24] While SIRT6 primarily removes long-chain acyl groups,[7,25] SIRT7 shows a preference for acidic modifications such as succinylation[26] or glutarylation.[27] These findings demonstrate the functional importance of sirtuin deacylation due to their remarkably broad substrate scope.

The superimposed experimental catalytic core structures of sirtuins (except hSIRT4, whose structure remains unresolved) are shown in Fig. 1. All sirtuins share a conserved ~275-amino acid catalytic core domain, while containing variable-length N-terminal and/or C-terminal extensions that confer unique structural features.[28] Structurally, sirtuins consist of two key subdomains: (1) a Rossmann fold domain responsible for NAD^+ binding and (2) a smaller zinc-binding domain. Between these subdomains lies a deep cleft that forms the binding pocket for both NAD^+ and the acylated substrate. The high degree of conservation in both the catalytic core architecture and the NAD^+-dependent reaction mechanism suggests that all sirtuins are likely to employ similar catalytic strategies for deacylation.

The enzymatic mechanism of sirtuin-mediated deacylation has been well established (Scheme 1) and proceeds through the

[a] *Institute of High Energy Physics, Chinese Academy of Sciences, Beijing 100000, People's Republic of China. E-mail: haoquan@ihep.ac.cn, qhao@hku.hk*
[b] *Spallation Neutron Source Science Center, Chinese Academy of Sciences, Dongguan 523000, People's Republic of China*
[c] *School of Biomedical Sciences, The University of Hong Kong, Hong Kong, China*

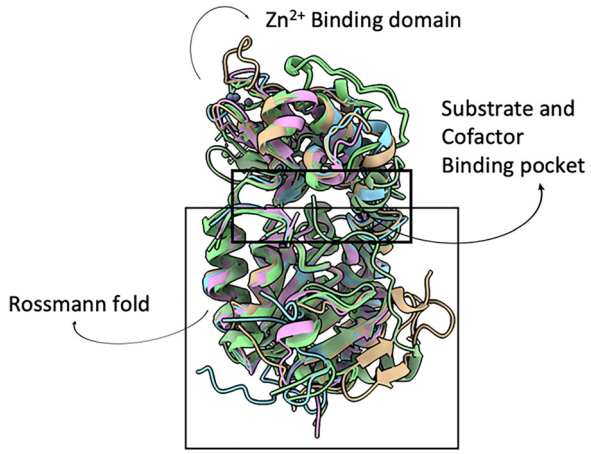

Fig. 1 Structural superposition of human sirtuin isoforms (SIRT1–3,5-7) based on conserved NAD^+-binding domains. SIRT1 (4IF6): tan, SIRT2 (6L66): light blue, SIRT3 (8H1W): plum, SIRT5 (4F4U): pale green, SIRT6 (3K35): dark sea green, SIRT7 (9GMK): pink.

following steps: (1) initial binding of cofactor NAD^+ to sirtuin-acylated substrate complex forms a ternary complex. (2) Cleavage of the nicotinamide–glycosidic bond releases the nicotinamide moiety. (3) The remaining NAD^+ fragment reacts with the acylated lysine substrate to form intermediate I.[29,30] (4) The key conserved catalytic histidine residue then deprotonates one of the hydroxyl groups of the reactive ribose ring, leading to formation of bicyclic intermediate II.[31] (5) The newly formed unstable five-membered ring breaks to generate intermediate III.[32] (6) Nucleophilic attack by water on intermediate III yields intermediate IV, which rapidly decomposes due to destabilization by three heteroatoms bound to a single carbon center, ultimately producing final product 2′-*O*-acyl-ADPR and deacylated peptide. Notably, several of these reaction intermediates have been structurally characterized using thioacetyl-lysine peptide analogs (as mechanism-based inhibitors), Carba-NAD^+ or on sirtuins from different species. Among these, analyses of pre-catalysis state have mainly used Carba-NAD^+, with studies conducted on both yeast sirtuin (yHst2)[33] and human SIRT2,[32] effectively mimicking the initial catalytic step under natural conditions. Although Carba-NAD^+ contains only a single modification (replacement of the ribose oxygen with carbon) and largely resembles the native state, the altered electronegativity of the modified ribose ring may influence either the binding conformation or atomic distances within the cofactor binding pocket. Structural characterization of sirtuin catalytic intermediates has been achieved through several key studies: intermediate I was captured in bacterial Sir2Tm complexed with thioacetyl peptides[30] and in human SIRT3 crystals containing acetyl-peptides, NAD^+, and the inhibitor Ex-243.[34] Intermediate II was first reported in studies of hSIRT5 with thiosuccinyl peptides.[31] Wang *et al.* subsequently identified intermediate III using hSIRT2/thiolmyristoyl complexes, revealing the subsequent mechanism after the formation of intermediates I and II.[32] Most of these reports focus on intermediate states I–III, and no structure of a pre-catalysis ternary complex in the native state has been reported; thus, the current structural basis is incomplete. In the current study, we employ X-ray crystallography and cryo-trapping methods to capture structural snapshots of pre-catalysis states with a native peptide substrate and NAD^+, to faithfully mimic physiological NAD^+-binding states. Additionally, our structural analysis explains the catalytic mechanism from the initial NAD^+ binding through pre-catalytic complex formation to nicotinamide–glycosidic bond cleavage. These findings provide a structural basis for completing the sirtuin catalysis mechanism cycle, and represent a crucial piece in this comprehensive dynamic process.

Results and discussion

Based on previous research, NAD^+-dependent deacylation is known to proceed *via* a sequential mechanism, wherein the acetylated substrate binds before NAD^+. Following the reaction, nicotinamide is released first, while OAADPr and the deacylated product are subsequently released in random order.[35] To understand the structural dynamics towards the formation of a pre-catalysis ternary complex, we employed X-ray crystallography and cryo-trapping techniques to capture snapshots of NAD^+ binding towards a myristoylated-peptide-bound SIRT2 binary complex. The soaking of NAD^+ into a peptide-bound SIRT2 co-crystal successfully

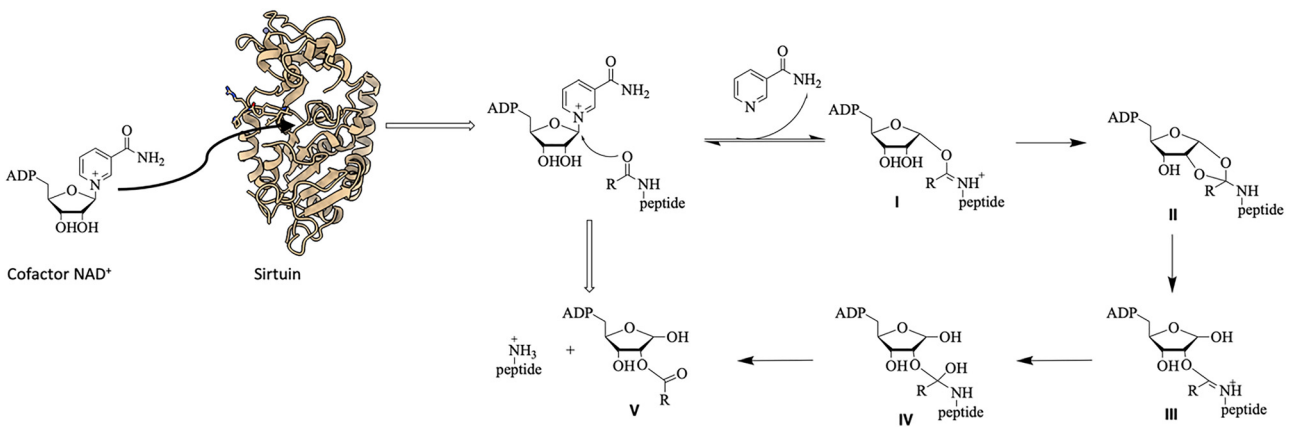

Scheme 1 The conserved enzymatic mechanism of sirtuin deacylation reactions. The structure of SIRT2 is used as a representative example.

revealed new conformations unknown to previous studies. Six structures were obtained, ranging from NAD^+-free (pre-soaking), the structures are presented chronologically to discuss the elucidated binding dynamics and cleavage mechanism. In addition,

Table 1 X-ray data collection and refinement statistics

	SIRT2-H3K18myr	SIRT2-H3K18myr: pre-NAD^+ binding state	SIRT2-H3K18myr-NAD^+: pre-catalysis state 1	SIRT2-H3K18myr-NAD^+: pre-catalysis state 2
PDB ID	9VG0	9VG3	9VEM	9VEW
Data collection				
Wavelength (Å)	0.97918	0.97861	0.97861	0.97861
Resolution[a] (Å)	27.81–1.61 (1.64–1.61)	53.75–2.15 (2.22–2.15)	55.25–2.57 (2.68–2.57)	55.31–2.68 (2.81–2.68)
Space group	$P12_11$	$P12_11$	$P12_11$	$P12_11$
Cell dimensions				
a, *b*, *c* (Å)	36.15, 73.50, 55.73	35.51, 72.53, 53.92,	37.86, 76.41, 55.64	37.92, 76.61, 55.71
α, β, γ (°)	90.00, 94.14, 90.00	90.00, 95.27, 90.00	90.00, 97.29, 90.00	90.00, 97.36, 90.00
Total reflections	221 899	102 163	69 547	61 226
Unique reflections	34 600	14 755	10 021	8852
Multiplicity	6.4	6.9	6.9	6.9
Completeness[a] (%)	91.8 (99.9)	99.0 (100.0)	99.2 (99.9)	98.8 (99.5)
Mean *I*/Sigma (*I*)[a]	17.1 (5.0)	14.2 (3.3)	7.1 (1.9)	10.6 (3.4)
Wilson *B*-factor (Å^2)	26.7	40.4	38.7	38.3
R_{meas}[a]	0.067 (0.455)	0.091 (0.637)	0.189 (1.116)	0.134 (0.585)
$CC_{1/2}$[a]	0.997 (0.939)	0.997 (0.876)	0.991 (0.767)	0.995 (0.922)
Refinement				
Reflections used in refinement	34 572	14 728	9950	8784
R_{work}/R_{free}	0.188/0.229	0.196/0.251	0.187/0.264	0.181/0.250
Number of atoms	2520	2409	2430	2419
Macromolecules/peptide	2267/44	2286/45	2250/46	2265/48
Ligands/ions	35/1	23/1	99/1	73/1
Water	173	54	34	32
rmsd bond lengths (Å)	0.0135	0.0058	0.0054	0.0072
rmsd bond angles (°)	1.903	1.573	1.498	1.750

	SIRT2-H3K18myr-NAD^+: pre-catalysis state 3	SIRT2 demyristoylation intermediate I structure	SIRT2-H3K18myr-NAD^+ H187A	SIRT2-H3K18myr-NAD^+ F96A
PDB ID	9V7W	9VGE	9VH0	9VGZ
Data collection				
Wavelength (Å)	0.97861	0.97861	0.97861	0.97918
Resolution[a] (Å)	44.9–1.86 (1.90–1.86)	55.47–2.56 (2.67–2.56)	47.08–2.41 (2.50–2.41)	45.21–2.34 (2.42–2.34)
Space group	$P12_11$	$P12_11$	*P*1	$P12_11$
Cell dimensions				
a, *b*, *c* (Å)	37.76, 76.57, 55.94	37.06, 77.65, 55.96	37.43, 48.13, 96.19	37.92, 77.13, 56.16
α, β, γ (°)	90.00, 97.88, 90.00	90.00, 97.99, 90.00	100.19, 91.58, 112.17	90.00, 97.11, 90.00
Total reflections	164 116	49 144	79 072	66 321
Unique reflections	26 232	9655	21 638	12 400
Multiplicity	6.3	5.1	3.7	5.3
Completeness[a] (%)	98.8 (93.6)	94.4 (81.3)	92.1 (86.9)	91.2 (97.5)
Mean *I*/Sigma (*I*)[a]	12.5 (0.2)	11.4 (3.4)	8.9 (2.0)	15.3 (6.6)
Wilson *B*-factor (Å^2)	29.3	41.9	37.6	41.69
R_{meas}[a]	0.112 (6.778)	0.180 (1.454)	0.072 (0.410)	0.083 (0.302)
$CC_{1/2}$[a]	0.999 (0.395)	0.994 (0.491)	0.995 (0.822)	0.995 (0.965)
Refinement				
Reflections used in refinement	26 214	9461	21 622	12 377
R_{work}/R_{free}	0.186/0.231	0.221/0.288	0.198/0.273	0.200/0.258
Number of atoms	2732	2406	4743	2495
Macromolecules/peptide	2481/49	2265/50	4496/87	2328/51
Ligands/ions	111/1	65/1	118/2	70/1
Water	90	25	40	45
rmsd bond lengths (Å)	0.0088	0.0203	0.0064	0.0150
rmsd bond angles (°)	1.846	1.736	1.656	1.899

[a] Value relative to the highest resolution shell are given in parentheses.

NAD^+-soaked (pre-binding), to NAD^+-bound (pre-catalytic) and intermediate I states. The last three states were differentiated by the absence, presence, and cleavage of NAD^+, respectively. Below, this study investigated Phe96 and His187, which are shown to affect the NAD^+-productive conformation *via* $SIRT2^{F96A}$ and $SIRT2^{H187A}$ mutants.

Comparison of apo SIRT2 and SIRT2/H3K18myr complex structures

Comparison of the structure of the SIRT2/H3K18myr complex and apo SIRT2 (PDB: 3ZGO) reveals that the myristoylated peptide binds directly in the large groove between the Rossmann fold domain and the zinc-binding domain, mirroring binding modes observed in other SIRT-peptide complexes.[6,36] The myristoylated lysine establishes key hydrogen bonds between its backbone NH/CO groups and Gly236/Glu237, while the myristoylated moiety inserts into the hydrophobic ligand binding pocket surrounded by aromatic residues, such as Phe96, Phe119, Phe131, Tyr139, Phe143, Phe190 and Phe235 (Fig. S1). This binding causes the amino acids near the ligand binding pocket to move closer to the peptide and provides a firm interaction with the peptide ligand. Additionally, the helix formed by Asp294 to Gly304 becomes flexible after the binding, and this region might stabilize through interaction with the bulkier native target of Sirt2.[37,38]

Zinc-binding domain opens and closes to capture NAD^+

The structure of human SIRT2 in complex with H3K18myr peptide was determined at 1.61 Å resolution without NAD^+ soaking (PDB: 9VG0, Table 1). To capture intermediate states, crystals were soaked with 10 mM native NAD^+ before flash-cooling, yielding structures of both the pre-NAD^+ binding state (PDB: 9VG3, 9 minutes) and pre-catalytic state 1 (PDB: 9VEM, 10 minutes). Soaking durations shorter than 9 minutes resulted in smeared diffraction spots (Fig. S2), suggesting that NAD^+ binding induces significant conformational changes, including a domain shift. After 10 min of soaking, the electron density of NAD^+ became clearly visible in the cofactor binding pocket, confirming complete occupancy (Fig. S3c–h). Superposition of these structures reveals that the zinc-binding domain undergoes an initial conformational shift to open the cofactor binding pocket, creating sufficient space for NAD^+ entry (Fig. 2(a), (c) and SI Movie S1). Subsequently, the zinc-domain shifts back, positioning NAD^+ deeply within the cofactor binding pocket (Fig. 2(b), (d) and SI Movie S2).

The hSIRT2–H3K18myr–NAD^+ ternary complex structure, at 2.57 Å resolution, reveals unambiguous electron density for NAD^+ (Fig. S3c). The cofactor is stabilized by an extensive hydrogen-bond network (Fig. 2(e)): (1) adenine and its attached ribose interact with Thr89, Asn286, Lys287 and Cys324 and (2) pyrophosphate contacts Ala85, Phe96, Arg97, Thr262 and Ser263. This binding mode positions the nicotinamide ribose proximal to the catalytic center, consistent with the established deacylation mechanism.

Key interactions to be focused on are related to the reactive moiety of NAD^+: (1) Ile169 and Asp170, as well as Ile93 and

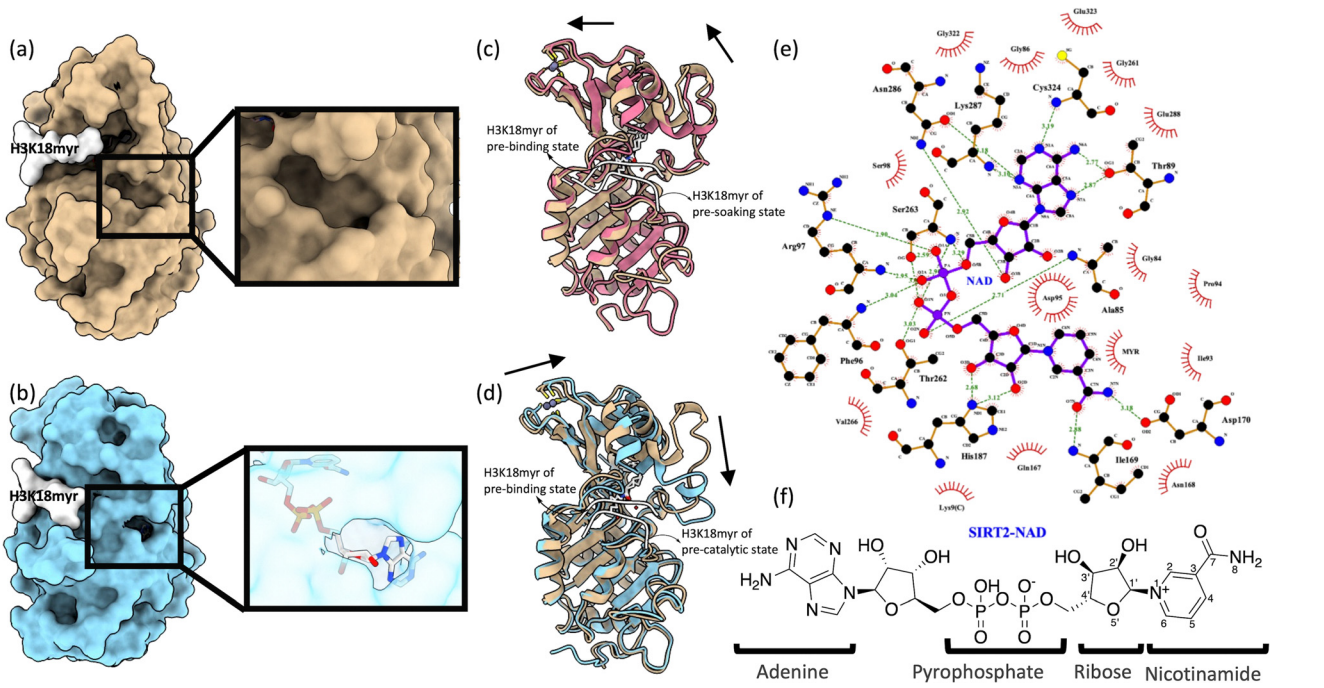

Fig. 2 Conformational changes of SIRT2 while NAD^+ binding. (a) Open state before NAD^+ binding (tan surface: pre-NAD^+ binding state of SIRT2, white surface: H3K18myr peptide). (b) Closed state after NAD^+ binding (light blue surface: binding state of SIRT2, white surface: H3K18myr peptide, light grey sticks: co-factor NAD^+). (c) The zinc-binding domain retracts to open the cofactor binding pocket from dark pink to tan (dark pink cartoon: SIRT2–H3K18myr peptide complex without NAD^+, tan cartoon: pre-NAD^+ binding SIRT2–H3K18myr complex), and (d) closures of cofactor binding pocket upon NAD^+ binding from tan to light blue; bold arrows indicate domain movement directions during the transition. (Movies of c and d are shown in Supplementary documents.) (e) LIGPLOT analysis of NAD^+–SIRT2 interactions. NAD^+ (purple bonds) and SIRT2 residues (orange bonds) are shown in ball-and-stick mode (C: black, N: blue, O: red, S: yellow). Hydrogen bonds (olive dashed lines) are labelled with distances (Å); hydrophobic interactions are shown by red arcs. Water molecules are omitted for clarity (detailed in subsequent figures). (f) Chemical structure and atom number of NAD^+.

Ala85 mediated by water, form hydrogen bonds with the carboxamide of nicotinamide (Fig. 3(b)). Meanwhile, (2) His187 of SIRT2 as well as the carbonyl oxygen of the myristoylated peptide substrate forms hydrogen bonds with 2′-OH and 3′-OH of the ribose ring (Fig. 2(e) and Fig. S4). These interactions collectively fix the nicotinamide ribose in the optimal orientation for catalysis while stabilizing NAD^+ in the cofactor binding site.

Aligning NAD^+ for nicotinamide cleavage

Two additional structures were solved in NAD^+-bound states: pre-catalysis states 2 (9VEW, 2.68 Å) and 3 (9V7W, 1.86 Å) were captured by increasing soaking time. States 1, 2 and 3 were defined based on the observed coordinates of NAD^+ proximity that show a gradual trend towards nicotinamide destabilization, corroborating the reaction mechanism. The global structure of these three complexes is largely unchanged, while local conformational shifts show subtle changes that optimize the NAD^+ position for nucleophilic attack. As shown in Fig. 3(b)–(d), the N atom of carboxamide in nicotinamide forms hydrogen bonds with Ile93 and Ala85 mediated by water. These interactions induce carboxamide distortion, disrupting its coplanarity with the aromatic ring and consequently destabilizing the electron delocalization of nicotinamide. This is one important reason behind the instability of NAD^+. The mechanism is supported by the observed gradual distortion of angle ∠(C4–C3–C7–N8) in pre-catalysis states 1–3 (Table 2), which shows an increasing trend (13.9° → 14.3° → 14.8°), consistent with carboxamide twisting. Concurrently, the recorded decreasing distance between the nicotinamide and Ile169 and Asp170 also indicates that NAD^+ is gradually pulled deeper into the cofactor binding pocket through hydrogen bonding.

In addition to the nicotinamide moiety, the 2′-OH and 3′-OH groups of the ribose ring are progressively moved away from His187, while the entire ribose is shifted toward the carbonyl oxygen of the myristoylated peptide, positioning itself in a favourable position for nucleophilic attack. In previous studies of sirtuin mechanisms, this highly conserved His187 has been proposed to act as a critical base, abstracting a proton from either 2′-OH or 3′-OH to facilitate the formation of intermediate I.[39]

Surprisingly, the pre-catalysis state structures (states 1–3) have been reported here, revealing a new ribose conformation. The electron density maps evidently show that His187 initially interacts with 3′-OH but not with 2′-OH. Across states 1–3, the ribose is gradually moved closer to the carbonyl oxygen of the myristoylated peptide, creating an electron-sufficient region (Fig. 3(k)). In this destabilized environment, the carboxamide twisting force can trigger the carbonyl oxygen of the myristoylated peptide to attack the 1′-carbon of the ribose, leading to nicotinamide cleavage and forming intermediate I. In this

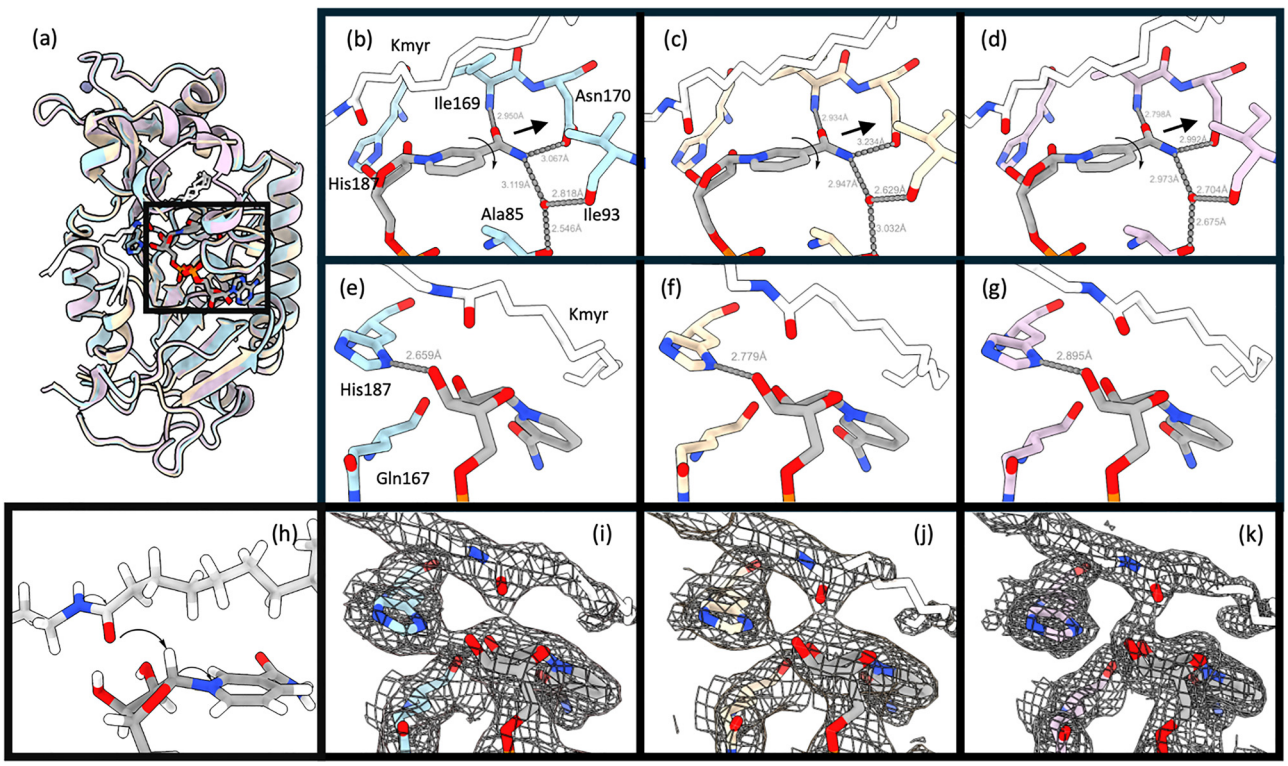

Fig. 3 NAD^+ alignment for nucleophilic attack. (a) Superimposition of pre-catalysis states 1–3, following time order, colored light blue, light brown, and light purple, respectively. NAD^+ is shown as light gray sticks and H3K18myr peptide is shown as white sticks. (b)–(g) Stereo diagram of nicotinamide moiety of NAD^+ (C: light gray, N: blue, O: red, P: orange) interact with H3K18myr peptide substrate and SIRT2. Hydrogen bonds (gray dashed lines) are labeled with distances (Å). (h) Structure-based mechanism of nicotinamide cleavage. (i)–(k) 2Fo-Fc electron density map contoured at 1σ of reactive SIRT2 amino acids, myristoylated peptide substrate and NAD^+.

Table 2 Distance and dihedral angle measurement

	Pre-catalysis state 1	Pre-catalysis state 2	Pre-catalysis state 3
NCA O-ILE169	2.950 Å	2.934 Å	2.798 Å
NCA N8-ASP170	3.067 Å	3.234 Å	2.992 Å
NCA N8-H_2O	3.119 Å	2.947 Å	2.973 Å
Dihedral angle ∠(C4–C3–C7–N8)	13.9°	14.3°	14.8°

mechanism, 2′-OH is activated, priming it for attack and ready to convert the intermediate to form intermediate II.

Nicotinamide cleavage occurred in SIRT2 ternary crystals

A post-cleavage complex (9VGE, 2.56 Å) was also obtained in this study after 12 minutes of NAD^+ soaking, indicating that the soaking system is catalytically active. A 2Fo-Fc omit map clearly defines the cleavage of nicotinamide and the covalent linkage formed between ADP-ribose and H3K18myr substrate (Fig. 4(c)), indicating that the complex is intermediate I of the catalytic cycle. Superposition of the pre-catalysis state 3 complex (9V7W) and post-cleavage structure complex (9VGE) reveals increased flexibility in the zinc-binding domain α-helix (Asp95–Ala117) near the active site (Fig. 4(a)). We speculate that this secondary structure change may facilitate opening of the cofactor binding pocket and product release.

Comparative analysis of the in-pocket structures before and after cleavage shows that the loop-attached Phe96 initially stacks above the ribose 5′-oxygen *via* π-electrons (Fig. 4(d)), positioning NAD^+ in the cofactor binding pocket and stabilizing the intermediate formed later. After cleavage, Phe96 is shifted in concert with the destabilization of the zinc-binding domain α-helix (Asp95–Ala117) to a loop structure, where the electron density of Tyr104–Tyr114 is not observed (Fig. 4(a)). The displacement of Phe96 suggests that Phe96 was shifted to release the constraint towards ribose, allowing the ribose to flip and form intermediate I with covalent linkage of peptide carbonyl oxygen and ribose 1′-carbon. Meanwhile, the helix-to-loop conformational shift increases the exposure of the binding pocket to the bulk solvent and is likely to promote the release of product at later stages.

Collectively, this series of structures has uncovered previously uncharacterized pre-catalytic dynamics, covering the window of NAD^+ binding and transition towards intermediate state I. Here, we propose mechanisms based on structural insights. Following cleavage and formation of intermediate I, electrons from the carbonyl oxygen migrate to the ribose 1′-carbon, forming a covalent bond. Meanwhile, the adenine

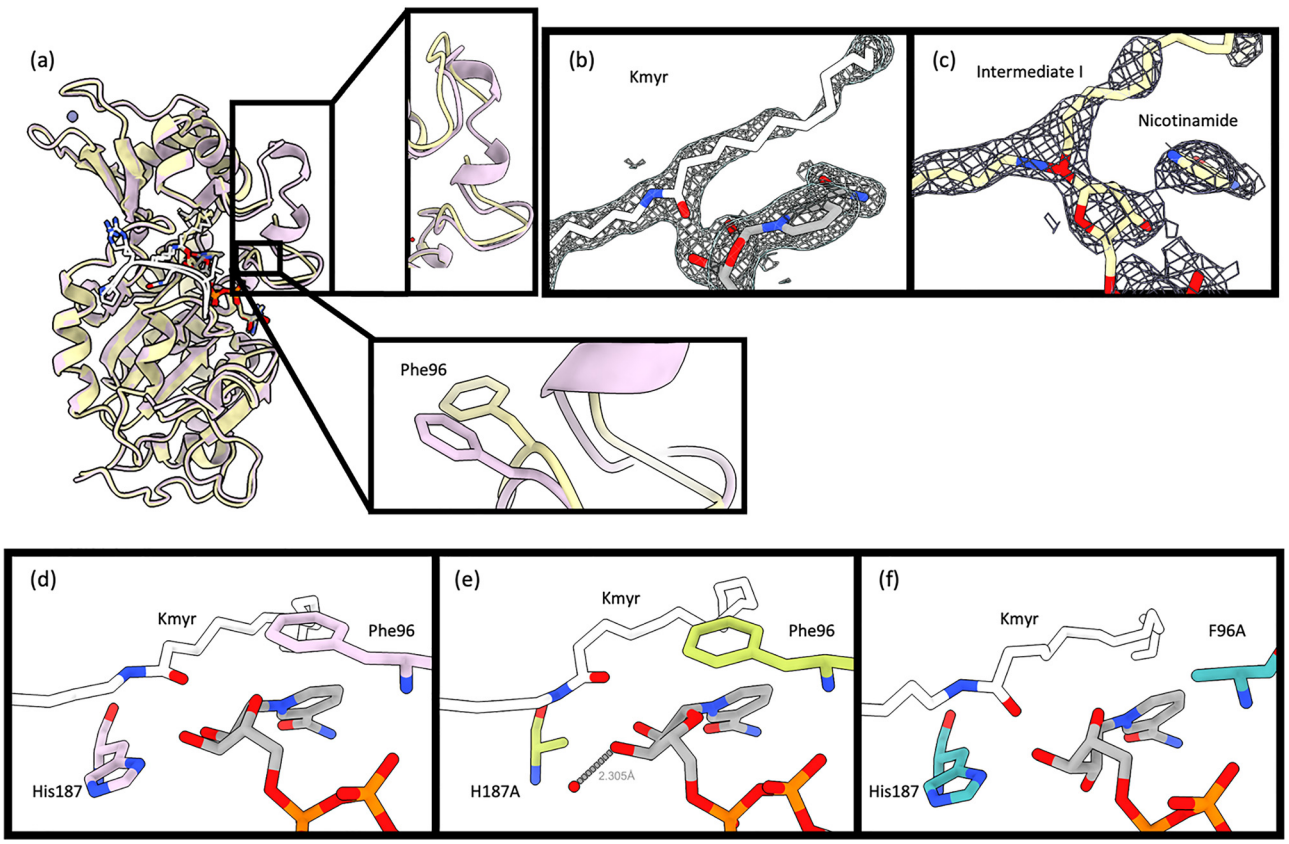

Fig. 4 (a) Superimposition of pre-catalysis state 3 with SIRT2-intermediate I complex (pale purple: pre-catalysis state 3, pale yellow: SIRT2-intermediate I complex). (b) and (c) 2Fo-Fc electron density map contoured at 1σ of myristoylated peptide substrate and NAD^+, before and after nicotinamide cleavage. (d) and (f) Cofactor NAD^+ (C: light grey, N: blue, O: red, P: orange), H3K18myr peptide (white) interact with SIRT2 WT (pale purple), H187A (olive), F96A (sea green). Water is shown as a red ball.

and pyrophosphate moieties remain largely stationary throughout this process. Therefore, the adenine and pyrophosphate moieties only act as a ''handle'' for NAD^+ cleavage, while nicotinamide is twisted by water-mediated hydrogen bonds, and the adjacent ribose is position-controlled by Phe96 and activated by His187, catalysing the enzymatic reaction.

Site-directed mutation: NAD^+-productive conformation relies on Phe96 more than His187

Previous studies have demonstrated that mutation of the highly conserved histidine in the sirtuin homologue significantly reduces enzymatic turnover.[40] Similarly, the homolog of Phe96, the 'gatekeeper' residue, was shown to be critical for deacetylation activity in yeast Sir2.[41] Corroborating previous studies, the proposed mechanism also highlights the essential roles of His187 and Phe96. To further investigate the function of Phe96 and His187, alanine-substituted mutants were constructed, and the ternary structures of $SIRT2^{H187A}$-H3K18myr-NAD^+ (9VH0, 2.41 Å) and $SIRT2^{F96A}$-H3K18myr-NAD^+ (9VGZ, 2.34 Å) were resolved and studied.

The electron density maps of both complexes are well resolved in the cofactor binding pocket (Fig. S3g and h), revealing different conformations in comparison to the productive state of the wild type (Fig. 4(d)–(f)). In the $SIRT2^{H187A}$-H3K18myr-NAD^+ complex, the NAD^+ ribose ring adopted a non-planar conformation slightly different from the wild-type structure. However, the 2′-OH and 3′-OH groups remain sufficiently proximal to the carbonyl oxygen of the myristoylated peptide. A water molecule is observed in place of His187, which is likely to functionally compensate for the missing His187 side chain.

In contrast, the conformation of the ribose ring in the $SIRT2^{F96A}$-H3K18myr-NAD^+ complex is displaced from the wild-type position, with a conformation distinctive from the productive one, restating the role of Phe96 in coordinating a productive conformation. Thus, NAD^+ conformation correction is largely dependent on Phe96 rather than His187.

Structural comparison with previously reported intermediate structures

In this study, we structurally characterized key stages of the sirtuin deacylation cycle, including the NAD^+-free (pre-soaking), NAD^+-soaked (pre-binding), NAD^+-bound (pre-catalytic) and intermediate I states. The NAD^+-soaked state represents a novel snapshot of NAD^+ entry into the active site. Afterwards, the overall SIRT2 structure shows no significant differences from the pre-catalytic state captured in hSIRT2 with carba-NAD^+ (PDB: 4X3P); however, the carbocyclic ribose ring in carba-NAD^+ is twisted away from Phe96 (Fig. S5a), consistent with our hypothesis that the interaction between Phe96 and the ribose 5′-O is essential for catalysis. Regarding the intermediate I states observed in hSIRT2, Sir2Tm, and hSIRT3, the ribose rings adopt distinct conformations; this flip might be caused by inhibitors employed in crystals (thioacetyl peptides in Sir2Tm and Ex-243 in SIRT3). Intermediate II and III states are also illustrated in (Fig. S5c and d). Collectively, along with previously reported intermediate states (II–III) trapped using mechanism-based inhibitors, these structures emulate a near-complete structural progression of the sirtuin deacylation reaction consuming NAD^+ within a crystalline environment *in vitro*.

Experimental

Recombinant SIRT2 and site-mutated SIRT2 protein expression and purification

The open reading frame of human SIRT2 (residues 50–356) was cloned into a pET28a-SUMO vector between the BamHI and XhoI restriction sites. Site-directed mutagenesis was performed on this construct using specific primers (Table S1) *via* IVA cloning.[42] For protein expression, *Escherichia coli* BL21(DE3)-RIL (EC1002) bacteria harboring expression plasmids were cultured aerobically in 2YT medium at 37 °C with the appropriate antibiotics (Kanamycin 50 mg mL^{-1}, chloramphenicol 34 mg mL^{-1}). When the culture reached an OD600 of 0.6–0.8, the expression of His-SUMO-tagged SIRT2 or its mutant was induced by adding 100 μM of isopropyl β-D-1-thiogalactopyranoside (IPTG), followed by incubation at 16 °C for 20 h. Later, the *E. coli* was collected by centrifugation, the liquid was discarded, and the pellet was resuspended in lysis buffer (500 mM NaCl, 20 mM sodium HEPES, pH 7.2, 0.1 mM phenylmethanesulfonyl fluoride) supplemented with EDTA-free protease inhibitor cocktail (InStab™), then lysed by sonication. After centrifugation, the supernatant was purified with a HisTrap HP column (Cytiva) with elution of 20–500 mM imidazole. By adding ULP1 protease, the protein solution mixture was purified with a HisTrap HP column followed by a HiTrap Q HP column (Cytiva) to get pure SIRT2 or site-mutated SIRT2 protein, and the purity of the desired protein was confirmed by SDS-PAGE. The final product was concentrated to 10 mg mL^{-1} and stored at −80 °C.

Crystallization of SIRT2 or site-mutated SIRT2 with H3K18myr complex

A solution of 10 mg mL^{-1} SIRT2 or site-mutated SIRT2 was pre-incubated with H3K18myr peptide (APRKmyrQLA; purchased from XTPEPTIDE, China) at a 1 : 4 ratio on ice for 1 h. The initial crystals were obtained by screening with commercial crystallization kits on a 96-well plate by a sitting-drop vapor diffusion method at 16 °C. Crystallization conditions were optimized to afford crystals of good quality. The final crystallography conditions of wild-type SIRT2 or $SIRT2^{F96A}$ are 0.1 M Tris, pH 8.0, 25% polyethylene glycol monomethyl ether 2000; while for $SIRT2^{H187A}$, they are 0.1 M MES, pH 5.5, 9.2% PEG 10 000. Larger crystals of the $SIRT2^{H187A}$ mutant were obtained through optimization using the Hampton seeding protocol, with microseeds introduced into the reservoir solution.

Preparation of SIRT2-H3K18myr-NAD^+ complexes

All complexes were obtained by soaking native SIRT2 crystals or $SIRT2^{F96A}$ or $SIRT2^{H187A}$ mutant crystals in solutions containing NAD^+. The NAD^+ solution was prepared at 10 mM in reservoir solution with the addition of 30% glycerol. The crystals were

soaked in prepared NAD^+ solution for 9 to 12 min at room temperature followed by cooling in liquid nitrogen. The crystals were carried to the Shanghai Synchrotron Radiation Facility (SSRF) for diffraction data collection.

Data collection, reduction, and structural refinement

X-ray diffraction data were collected at beamlines 10U2 or 19U1 of the Shanghai Synchrotron Radiation Facility (SSRF) under cryogenic conditions (100 K) using a wavelength of 0.979 Å. Complete datasets were acquired through 360° rotations with 1° oscillation per image.

Data processing was performed using the XDS package,[43] followed by scaling and reduction with AIMLESS[44] within the CCP4i2 suite.[45] Initial phase determination was achieved by molecular replacement using PHASER[46] with PDB entry 4X3O[32] as the search model. The SIRT2-intermediate I structure was obtained by model rebuilding through BUCCANEER.[47] The other structures were resolved using the SIRT2-H3K18myr peptide structure (9VG0) as the search model. Structural refinement was conducted through alternating cycles of automated refinement in REFMAC5[48] and manual adjustment in Coot.[49] PDB-REDO[50,51] was also used for structural optimization. Final refinement included translation–libration–screw (TLS) parameterization before deposition in the Protein Data Bank. Data collection and refinement statistics are summarized in Table 1.

Structural analyses and visualization were performed using UCSF ChimeraX.[52] Protein–ligand interactions were analyzed using LIGPLOT+.[53,54]

Conclusions

The structures from the SIRT2-H3K18myr complex *via* the pre-NAD^+ binding state to ternary SIRT2-H3K18myr-NAD^+ have revealed the dynamic process of zinc-binding domain shifting of sirtuin–NAD^+ binding. The structures of pre-catalysis states 1–3 have provided direct evidence addressing the key question of the nicotinamide cleavage mechanism, which is initiated by the disruption of the carboxamide–aromatic ring resonance through water-bridged hydrogen bonds formed with Ile93 and Ala85. These structures also illustrate novel pre-catalysis states before the formation of intermediate I. The structure of SIRT2-intermediate I faithfully mimics the physiological NAD^+-binding process and affords one native intermediate state, indicating that in-crystal studies of an enzymatic process are possible. Complementary mutagenesis studies confirm the functional importance of Phe96 and His187 in stabilizing NAD^+ in its productive conformation rather than NAD^+ recognition.

Author contributions

Experimental design: N. Z., L. C. Q. H.; crystallization and data processing: N. Z.; data collection: N. Z., K.-C. P.; data analysis: N. Z., K.-C. P.; manuscript preparation: N. Z., K.-C. P., Q. H.; supervision: Q. H.

Conflicts of interest

There are no conflicts to declare.

Data availability

Atomic coordinates and structure factors have been deposited with the PDB database under accession codes: 9VG0 (SIRT2 structure in complex with H3K18myr peptide); 9VG3 (SIRT2 structure in complex with H3K18myr peptide: pre-NAD^+ binding state); 9VEM (SIRT2 structure in complex with H3K18myr peptide and native NAD^+: pre-catalysis state 1); 9VEW (SIRT2 structure in complex with H3K18myr peptide and native NAD^+: pre-catalysis state 2); 9V7W (SIRT2 structure in complex with H3K18myr peptide and native NAD^+: pre-catalysis state 3); 9VGE (SIRT2 demyristoylation intermediate I structure); 9VH0 (SIRT2-H187A structure in complex with H3K18myr peptide and native NAD^+); 9VGZ (SIRT2-F96A structure in complex with H3K18myr peptide and native NAD^+).

Supplementary figures and movies are available. See DOI: https://doi.org/10.1039/d5cb00169b.

Acknowledgements

We would like to thank the Shanghai Synchrotron Radiation Facility staff members for their support and Ming Yan for stimulating discussions and help with data collection. This work was supported by Basic and Applied Basic Research Foundation of Guangdong Province (grant no. 2023B0303000003).

References

1 S. Zhao, W. Xu, W. Jiang, W. Yu, Y. Lin, T. Zhang, J. Yao, L. Zhou, Y. Zeng, H. Li, Y. Li, J. Shi, W. An, S. M. Hancock, F. He, L. Qin, J. Chin, P. Yang, X. Chen, Q. Lei, Y. Xiong and K.-L. Guan, *Science*, 2010, **327**, 1000–1004.
2 Y. L. Deribe, T. Pawson and I. Dikic, *Nat. Struct. Mol. Biol.*, 2010, **17**, 666–672.
3 J. Brustel, T. Muramoto, K. Fumimoto, J. Ellins, C. J. Pears and N. D. Lakin, *Nat. Commun.*, 2022, **13**, 185.
4 P. Bheda, J. T. Wang, J. C. Escalante-Semerena and C. Wolberger, *Protein Sci.*, 2011, **20**, 131–139.
5 J. L. Feldman, J. Baeza and J. M. Denu, *J. Biol. Chem.*, 2013, **288**, 31350–31356.
6 Y.-B. Teng, H. Jing, P. Aramsangtienchai, B. He, S. Khan, J. Hu, H. Lin and Q. Hao, *Sci. Rep.*, 2015, **5**, 8529.
7 H. Jiang, S. Khan, Y. Wang, G. Charron, B. He, C. Sebastian, J. Du, R. Kim, E. Ge, R. Mostoslavsky, H. C. Hang, Q. Hao and H. Lin, *Nature*, 2013, **496**, 110–113.
8 C. Peng, Z. Lu, Z. Xie, Z. Cheng, Y. Chen, M. Tan, H. Luo, Y. Zhang, W. He, K. Yang, B. M. M. Zwaans, D. Tishkoff, L. Ho, D. Lombard, T.-C. He, J. Dai, E. Verdin, Y. Ye and Y. Zhao, *Mol. Cell. Proteomics*, 2011, **10**(12), M111.012658.
9 J. Du, Y. Zhou, X. Su, J. J. Yu, S. Khan, H. Jiang, J. Kim, J. Woo, J. H. Kim, B. H. Choi, B. He, W. Chen, S. Zhang,

R. A. Cerione, J. Auwerx, Q. Hao and H. Lin, *Science*, 2011, **334**, 806–809.
10 M. Tan, C. Peng, K. A. Anderson, P. Chhoy, Z. Xie, L. Dai, J. Park, Y. Chen, H. Huang, Y. Zhang, J. Ro, G. R. Wagner, M. F. Green, A. S. Madsen, J. Schmiesing, B. S. Peterson, G. Xu, O. R. Ilkayeva, M. J. Muehlbauer, T. Braulke, C. Mühlhausen, D. S. Backos, C. A. Olsen, P. J. McGuire, S. D. Pletcher, D. B. Lombard, M. D. Hirschey and Y. Zhao, *Cell Metab.*, 2014, **19**, 605–617.
11 Z. Fan, Z. Liu, N. Zhang, W. Wei, K. Cheng, H. Sun and Q. Hao, *iScience*, 2023, **26**(10), 107757.
12 X. Zhang, R. Cao, J. Niu, S. Yang, H. Ma, S. Zhao and H. Li, *Cell Discovery*, 2019, **5**, 35.
13 L. Perico, M. Morigi, A. Pezzotta, D. Corna, V. Brizi, S. Conti, C. Zanchi, F. Sangalli, P. Trionfini, S. Buttò, C. Xinaris, S. Tomasoni, C. Zoja, G. Remuzzi, A. Benigni and B. Imberti, *Sci. Rep.*, 2021, **11**, 23580.
14 R. A. Frye, *Biochem. Biophys. Res. Commun.*, 2000, **273**, 793–798.
15 E. Michishita, J. Y. Park, J. M. Burneskis, J. C. Barrett and I. Horikawa, *Mol. Biol. Cell*, 2005, **16**, 4623–4635.
16 A. Vaquero, M. B. Scher, D. H. Lee, A. Sutton, H. L. Cheng, F. W. Alt, L. Serrano, R. Sternglanz and D. Reinberg, *Genes Dev.*, 2006, **20**, 1256–1261.
17 B. Schwer, B. J. North, R. A. Frye, M. Ott and E. Verdin, *J. Cell Biol.*, 2002, **158**, 647–657.
18 K. Tanabe, J. Liu, D. Kato, H. Kurumizaka, K. Yamatsugu, M. Kanai and S. A. Kawashima, *Sci. Rep.*, 2018, **8**, 2656.
19 X. Bao, Y. Wang, X. Li, X.-M. Li, Z. Liu, T. Yang, C. F. Wong, J. Zhang, Q. Hao and X. D. Li, *eLife*, 2014, **3**, e02999.
20 J. L. Feldman, J. Baeza and J. M. Denu, *J. Biol. Chem.*, 2013, **288**, 31350–31356.
21 R. A. Mathias, T. M. Greco, A. Oberstein, H. G. Budayeva, R. Chakrabarti, E. A. Rowland, Y. Kang, T. Shenk and I. M. Cristea, *Cell*, 2014, **159**, 1615–1625.
22 K. A. Anderson, F. K. Huynh, K. Fisher-Wellman, J. D. Stuart, B. S. Peterson, J. D. Douros, G. R. Wagner, J. W. Thompson, A. S. Madsen, M. F. Green, R. M. Sivley, O. R. Ilkayeva, R. D. Stevens, D. S. Backos, J. A. Capra, C. A. Olsen, J. E. Campbell, D. M. Muoio, P. A. Grimsrud and M. D. Hirschey, *Cell Metab.*, 2017, **25**, 838–855.
23 N. G. Simonet, J. K. Thackray, B. N. Vazquez, A. Ianni, M. Espinosa-Alcantud, J. Morales-Sanfrutos, S. Hurtado-Bagès, E. Sabidó, M. Buschbeck, J. Tischfield, C. De La Torre, M. Esteller, T. Braun, M. Olivella, L. Serrano and A. Vaquero, *Sci. Adv.*, 2020, **6**, eaaz2590.
24 G. Liszt, E. Ford, M. Kurtev and L. Guarente, *J. Biol. Chem.*, 2005, **280**, 21313–21320.
25 X. Zhang, S. Khan, H. Jiang, M. A. Antonyak, X. Chen, N. A. Spiegelman, J. H. Shrimp, R. A. Cerione and H. Lin, *Nat. Chem. Biol.*, 2016, **12**, 614–620.
26 L. Li, L. Shi, S. Yang, R. Yan, D. Zhang, J. Yang, L. He, W. Li, X. Yi, L. Sun, J. Liang, Z. Cheng, L. Shi, Y. Shang and W. Yu, *Nat. Commun.*, 2016, **7**, 12235.
27 X. Bao, Z. Liu, W. Zhang, K. Gladysz, Y. M. E. Fung, G. Tian, Y. Xiong, J. W. H. Wong, K. W. Y. Yuen and X. D. Li, *Mol. Cell*, 2019, **76**, 660–675.
28 S. Michan and D. Sinclair, *Biochem. J.*, 2007, **404**, 1–13.
29 L. Jin, W. Wei, Y. Jiang, H. Peng, J. Cai, C. Mao, H. Dai, W. Choy, J. E. Bemis, M. R. Jirousek, J. C. Milne, C. H. Westphal and R. B. Perni, *J. Biol. Chem.*, 2009, **284**, 24394–24405.
30 W. F. Hawse, K. G. Hoff, D. G. Fatkins, A. Daines, O. V. Zubkova, V. L. Schramm, W. Zheng and C. Wolberger, *Structure*, 2008, **16**, 1368–1377.
31 Y. Zhou, H. Zhang, B. He, J. Du, H. Lin, R. A. Cerione and Q. Hao, *J. Biol. Chem.*, 2012, **287**, 28307–28314.
32 Y. Wang, Y. M. E. Fung, W. Zhang, B. He, M. W. H. Chung, J. Jin, J. Hu, H. Lin and Q. Hao, *Cell Chem. Biol.*, 2017, **24**, 339–345.
33 K. Zhao, R. Harshaw, X. Chai and R. Marmorstein, *Proc. Natl. Acad. Sci. U. S. A.*, 2004, **101**, 8563–8568.
34 M. Gertz, F. Fischer, G. T. Nguyen, M. Lakshminarasimhan, M. Schutkowski, M. Weyand and C. Steegborn, *Proc. Natl. Acad. Sci. U. S. A.*, 2013, **110**, E2772–E2781.
35 M. T. Borra, M. R. Langer, J. T. Slama and J. M. Denu, *Biochemistry*, 2004, **43**, 9877–9887.
36 J. Du, Y. Zhou, X. Su, J. J. Yu, S. Khan, H. Jiang, J. Kim, J. Woo, J. H. Kim, B. H. Choi, B. He, W. Chen, S. Zhang, R. A. Cerione, J. Auwerx, Q. Hao and H. Lin, *Science*, 2011, **334**, 806–809.
37 C. Moreno-Yruela, B. E. Ekundayo, P. N. Foteva, D. Ni, E. Calvino-Sanles, H. Stahlberg and B. Fierz, *Nat. Commun.*, 2025, **16**, 1328.
38 E. Smirnova, E. Bignon, P. Schultz, G. Papai and A. Ben Shem, *eLife*, 2024, **12**, RP87989.
39 K. G. Hoff, J. L. Avalos, K. Sens and C. Wolberger, *Structure*, 2006, **14**, 1231–1240.
40 M. D. Jackson, M. T. Schmidt, N. J. Oppenheimer and J. M. Denu, *J. Biol. Chem.*, 2003, **278**, 50985–50998.
41 C. M. Armstrong, M. Kaeberlein, S. I. Imai and L. Guarente, *Mol. Biol. Cell*, 2002, **13**, 1427–1438.
42 J. García-Nafría, J. F. Watson and I. H. Greger, *Sci. Rep.*, 2016, **6**, 27459.
43 W. Kabsch, *Acta Crystallogr., Sect. D: Biol. Crystallogr.*, 2010, **66**, 125–132.
44 P. R. Evans and G. N. Murshudov, *Acta Crystallogr., Sect. D: Biol. Crystallogr.*, 2013, **69**, 1204–1214.
45 M. D. Winn, C. C. Ballard, K. D. Cowtan, E. J. Dodson, P. Emsley, P. R. Evans, R. M. Keegan, E. B. Krissinel, A. G. Leslie, A. McCoy, S. J. McNicholas, G. N. Murshudov, N. S. Pannu, E. A. Potterton, H. R. Powell, R. J. Read, A. Vagin and K. S. Wilson, *Acta Crystallogr., Sect. D: Biol. Crystallogr.*, 2011, **67**, 235–242.
46 A. J. McCoy, R. W. Grosse-Kunstleve, P. D. Adams, M. D. Winn, L. C. Storoni and R. J. Read, *J. Appl. Crystallogr.*, 2007, **40**, 658–674.
47 K. Cowtan, *Acta Crystallogr., Sect. D: Biol. Crystallogr.*, 2012, **68**, 328–335.
48 A. A. Vagin, R. A. Steiner, A. A. Lebedev, L. Potterton, S. McNicholas, F. Long and G. N. Murshudov, *Acta Crystallogr., Sect. D: Biol. Crystallogr.*, 2004, **60**, 2184–2195.

49 P. Emsley, B. Lohkamp, W. G. Scott and K. Cowtan, *Acta Crystallogr., Sect. D: Biol. Crystallogr.*, 2010, **66**, 486–501.
50 R. P. Joosten, F. Long, G. N. Murshudov and A. Perrakis, *IUCrJ*, 2014, **1**, 213–220.
51 W. G. Touw, B. van Beusekom, J. M. Evers, G. Vriend and R. P. Joosten, *Acta Crystallogr., Sect. D: Biol. Crystallogr.*, 2016, **72**, 1110–1118.
52 E. F. Pettersen, T. D. Goddard, C. C. Huang, E. C. Meng, G. S. Couch, T. I. Croll, J. H. Morris and T. E. Ferrin, *Protein Sci.*, 2021, **30**, 70–82.
53 R. A. Laskowski and M. B. Swindells, *J. Chem. Inf. Model.*, 2011, **51**, 2778–2786.
54 A. C. Wallace, R. A. Laskowski and J. M. Thornton, *Protein Eng.*, 1995, **8**, 127–134.